

<https://doi.org/10.1038/s42003-024-06245-y>

# Fluorescence imaging sheds light on the immune evasion mechanisms of hepatic stellate cells mediated by superoxide anion

Check for updates

Yuantao Mao<sup>1,4</sup>, Chuanchen Wu<sup>1,4</sup>, Xin Wang<sup>1</sup> , Fanghui Zhang<sup>1</sup>, Xinru Qi<sup>1</sup>, Xia Li<sup>2</sup> , Ping Li<sup>1</sup> & Bo Tang<sup>1,3</sup>

Whether and how the reactive oxygen species generated by hepatic stellate cells (HSCs) promote immune evasion of hepatocellular carcinoma (HCC) remains mysterious. Therefore, investigating the function of superoxide anion ( $O_2^{\bullet-}$ ), the firstly generated reactive oxygen species, during the immune evasion become necessary. In this work, we establish a novel in situ imaging method for visualization of  $O_2^{\bullet-}$  changes in HSCs based on a new two-photon fluorescence probe TPH. TPH comprises recognition group for  $O_2^{\bullet-}$  and HSCs targeting peptides. We observe that  $O_2^{\bullet-}$  in HSCs gradually rose, impairing the infiltration of  $CD8^+$  T cells in HCC mice. Further studies reveal that the cyclin-dependent kinase 4 is deactivated by  $O_2^{\bullet-}$ , and then cause the up-regulation of PD-L1. Our work provides molecular insights into HSC-mediated immune evasion of HCC, which may represent potential targets for HCC immunotherapy.

Hepatocellular carcinoma (HCC) is the fourth leading cause of cancer-related death, posing a serious threat to people's health and lives<sup>1,2</sup>. In recent decades, a variety of immunotherapy strategies have been developed for the treatment of HCC<sup>3,4</sup>. Although have shown great promises, their clinical therapeutic efficacy was reduced by the immune evasion<sup>3</sup>. Immune evasion refers to the process through which cancer cells inhibit or decrease the body's immune response to malignancy. Undoubtedly, immune evasion is regarded as an indispensable strategy for HCC cell survival<sup>5,6</sup>. Immune evasion in HCC complicates the treatment, and also increases the risk of tumor metastasis and postoperative recurrence. Therefore, understanding the molecular mechanism of immune evasion can provide vital insight for HCC treatment.

Hepatic stellate cells (HSCs) account for 10% of the nonparenchymal cells in the liver. HSCs are crucial mediators in regulating the physiological and pathological processes of liver<sup>7</sup>. When stimulated by injuries or immune responses, the HSCs in quiescent state transform into active state (aHSCs)<sup>8</sup>. Subsequently, aHSCs regulate liver fibrosis and immune processes via

secreting active molecules such as the extracellular matrix, cytokines, and reactive oxygen species (ROS) through lipid metabolism<sup>9,10</sup>. Current studies have shown that abnormal aHSCs could cause the immune evasion of HCC cells<sup>11–13</sup>. Couloarn et al. found that HCC cells upregulated the expression of vascular endothelial growth factor A in HSCs, causing the promotion of angiogenesis at tumor sites<sup>12</sup>. In addition, aHSCs promoted migration and invasion of HCC cells through focal adhesion kinase-matrix metalloproteinase 9 signaling<sup>13</sup>. However, the detailed molecular mechanisms still need to be explored.

Superoxide anion ( $O_2^{\bullet-}$ ), as the first ROS produced in organisms, profoundly affects the immune responses of HCC<sup>14,15</sup>. The activation of HSCs is accompanied by lipid metabolism and oxidative phosphorylation, providing energy to maintain the normal physiological functions of the cells. Importantly, oxidative phosphorylation is an important pathway to produce  $O_2^{\bullet-}$ . Therefore, we assume that during this process, the levels of  $O_2^{\bullet-}$  may change distinctly. However, due to the high activity and short duration of  $O_2^{\bullet-}$ , no suitable method for real-time and in situ

<sup>1</sup>College of Chemistry, Chemical Engineering and Materials Science, Collaborative Innovation Center of Functionalized Probes for Chemical Imaging in Universities of Shandong, Key Laboratory of Molecular and Nano Probes, Ministry of Education, Institute of Biomedical Sciences, Shandong Normal University, Jinan 250014, China. <sup>2</sup>Innovative Institute of Chinese Medicine and Pharmacy, Shandong University of Traditional Chinese Medicine, Jinan, China. <sup>3</sup>Laoshan Laboratory, 168 Wenhai Middle Rd, Aoshanwei Jimo, Qingdao 266237 Shandong, China. <sup>4</sup>These authors contributed equally: Yuantao Mao, Chuanchen Wu.

e-mail: [xinwang@sdu.edu.cn](mailto:xinwang@sdu.edu.cn); [60230033@sdu.edu.cn](mailto:60230033@sdu.edu.cn); [lip@sdu.edu.cn](mailto:lip@sdu.edu.cn); [tangb@sdu.edu.cn](mailto:tangb@sdu.edu.cn)

**Fig. 1 | Structure and recognition mechanism of TPH.** The catechol unit of the caffeic acid in the probe is an electron-donating group, and upon reaction with  $O_2^{\cdot-}$ , the catechol is oxidized to an electron-absorbing quinone structure, which redistributes the electrons within the molecule, resulting in intense fluorescence.

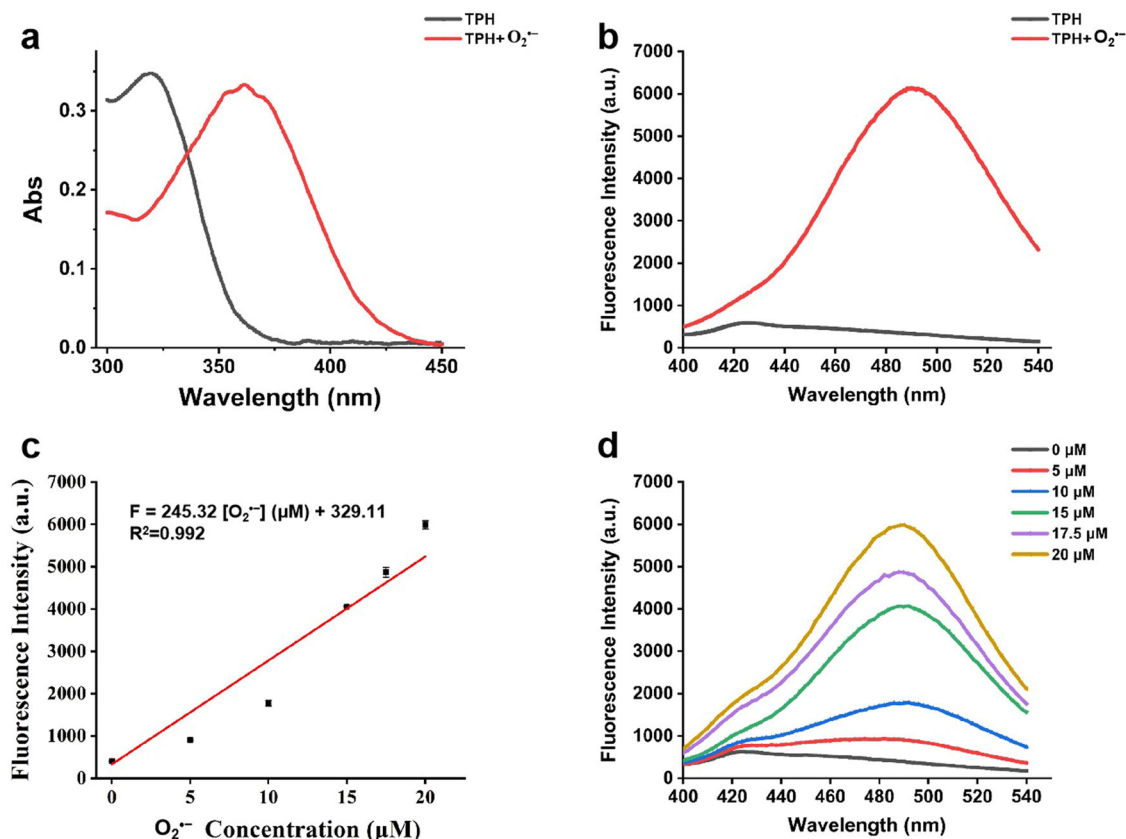
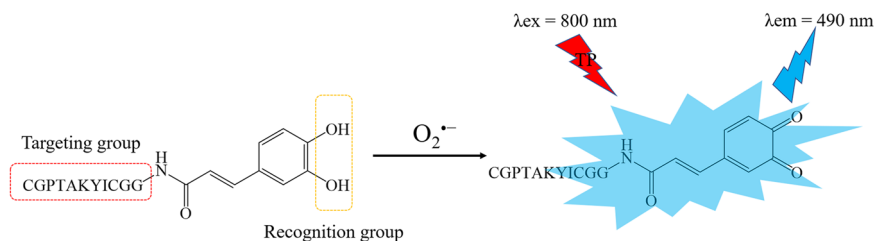


**Fig. 2 | Optical properties of TPH.** **a, b** Absorption and fluorescence spectra before and after the reaction of 20  $\mu M$  TPH with 20  $\mu M$   $O_2^{\cdot-}$ . **c** Linear relationship between fluorescence intensities and  $O_2^{\cdot-}$  concentrations (0–20  $\mu M$ ). **d** Fluorescence spectra of 20  $\mu M$  TPH in response to various concentrations of  $O_2^{\cdot-}$ .

detecting  $O_2^{\cdot-}$  in HSCs has been reported. Thus, whether and how  $O_2^{\cdot-}$  produced in aHSCs regulate immune evasion of HCC remains mysterious. Therefore, it is urgent to develop a tool that can be used to explore the flux of  $O_2^{\cdot-}$  in HSCs, and investigate the detailed mechanism of HCC immune evasion mediated by  $O_2^{\cdot-}$ .

Currently, two-photon fluorescence imaging technique with high sensitivity and real-time detection has served as a superior approach to monitor molecule events in vitro and in vivo<sup>16–18</sup>. This technique has excellent repeatability, and can greatly avoid the interference of biological tissue absorption by its two-photon absorption property. With the help of two-photon fluorescence imaging technique, our group had observed the dynamic, reversible changes of  $O_2^{\cdot-}$  in the liver injury mediated by ischemia-reperfusion and in brains of mice with depression<sup>17,18</sup>. However, there is still a lack of imaging material for two-photon fluorescence imaging of  $O_2^{\cdot-}$  level changes in HSCs.

To solve the above problems, we designed a two-photon fluorescence probe TPH for imaging  $O_2^{\cdot-}$  in HSCs. TPH was composed of CGPTAKYIC<sup>19</sup> for HSCs-specific targeting and caffeic acid residue as a recognition group for specific detection of  $O_2^{\cdot-}$ . In the presence of  $O_2^{\cdot-}$ , caffeic acid residues undergo phenol–quinone tautomerization, resulting in

enhanced fluorescence (Fig. 1). Using TPH, we investigated the function of  $O_2^{\cdot-}$  during the activation of HSCs in vitro and in vivo. Further research found that excess  $O_2^{\cdot-}$  caused dysfunction of cyclin-dependent kinase 4 (CDK4), which in turn led to increased programmed cell death-ligand 1 (PD-L1) levels. Ultimately, these changes promoted the immune evasion of HCC.

## Results and discussion

### Optical properties of TPH

The synthesis and structural characterizations of TPH were shown in Supplementary Figs. 1–3. Prior to the in vivo application, we investigated the photophysical properties of TPH. As shown in Fig. 2a, the absorption maximum peak of TPH was 320 nm, which would shift to 370 nm after reacting with  $O_2^{\cdot-}$ . Next, the fluorescence response of TPH to  $O_2^{\cdot-}$  was tested. The addition of  $O_2^{\cdot-}$  resulted in an increased fluorescence intensity due to the oxidation of the phenolic hydroxyl group in TPH by  $O_2^{\cdot-}$  (Fig. 2b). The fluorescence intensities of TPH at 490 nm increased gradually as  $O_2^{\cdot-}$  was added in the range of 0–20  $\mu M$ . The linear equation was  $F = 245.32 [O_2^{\cdot-}] (\mu M) + 329.11$ , with a linear correlation coefficient of 0.992. The limit of detection (LOD) was 111 nM, as calculated by the

equation  $LOD = 3\sigma/K$  (Fig. 2c, d). To interrogate the specificity of TPH toward  $O_2^{\cdot-}$ , we examined the fluorescence responses of TPH to  $O_2^{\cdot-}$  and other common interfering substances under simulated physiological conditions. The probe can also recognize  $O_2^{\cdot-}$  under two-photon excitation of 800 nm (Supplementary Fig. 4). Encouragingly, only  $O_2^{\cdot-}$  resulted in a significant increase of the fluorescence signal at 490 nm without any interference from other highly active molecules in vivo (Supplementary Fig. 5). This suggested that TPH showed excellent specificity to  $O_2^{\cdot-}$ . Moreover, TPH exhibits the reversible response to  $O_2^{\cdot-}$ . In addition, TPH possessed other advantages including instantaneous response, good photostability and favorable biocompatibility (Supplementary Figs. 6–12). The above results highlight that the probe could be a promising candidate for  $O_2^{\cdot-}$  detection during the activation of HSCs.

### $O_2^{\cdot-}$ detection during the activation of HSCs

Motivated by the preminent photophysical properties of TPH, we explored its capability of imaging  $O_2^{\cdot-}$  during the activation of HSCs. Cell selectivity experiments confirmed that TPH could specifically target HSCs (Supplementary Fig. 13). First, we verified whether the TPH could recognize  $O_2^{\cdot-}$  in HSCs. LX-2 cells were pretreated with 2-methoxyestradiol (2-Me) to boost the endogenous  $O_2^{\cdot-}$  level<sup>20,21</sup>. As shown in Fig. 3a, b, compared with the control group, 2-Me treated cells elicited brighter fluorescence. In contrast, the fluorescence intensity was significantly reduced when Tiron ( $O_2^{\cdot-}$  scavenger) was added to those cells<sup>22</sup>. These images illustrated that  $O_2^{\cdot-}$  in HSCs could be tested by TPH. Subsequently, we explored the changes of  $O_2^{\cdot-}$  levels during the activation of HSCs. We successfully activated hepatic stellate cells using TGF- $\beta$ 1 (Supplementary Fig. 14)<sup>23</sup>. As displayed in Fig. 3c, d, cells with TGF- $\beta$ 1 incubation showed significantly increased fluorescence compared with the control group. Moreover, the fluorescence intensity of the Tiron group was lower than that of the TGF- $\beta$ 1 group. Moreover, the imaging results of  $O_2^{\cdot-}$  level changes during HSCs activation could be stimulated performed under both one-photon and two-photon excitations (Supplementary Fig. 15).

The finding indicated that a large amount of  $O_2^{\cdot-}$  was produced during the activation of HSCs. Overall, we successfully established an imaging method for detecting  $O_2^{\cdot-}$  within HSCs.

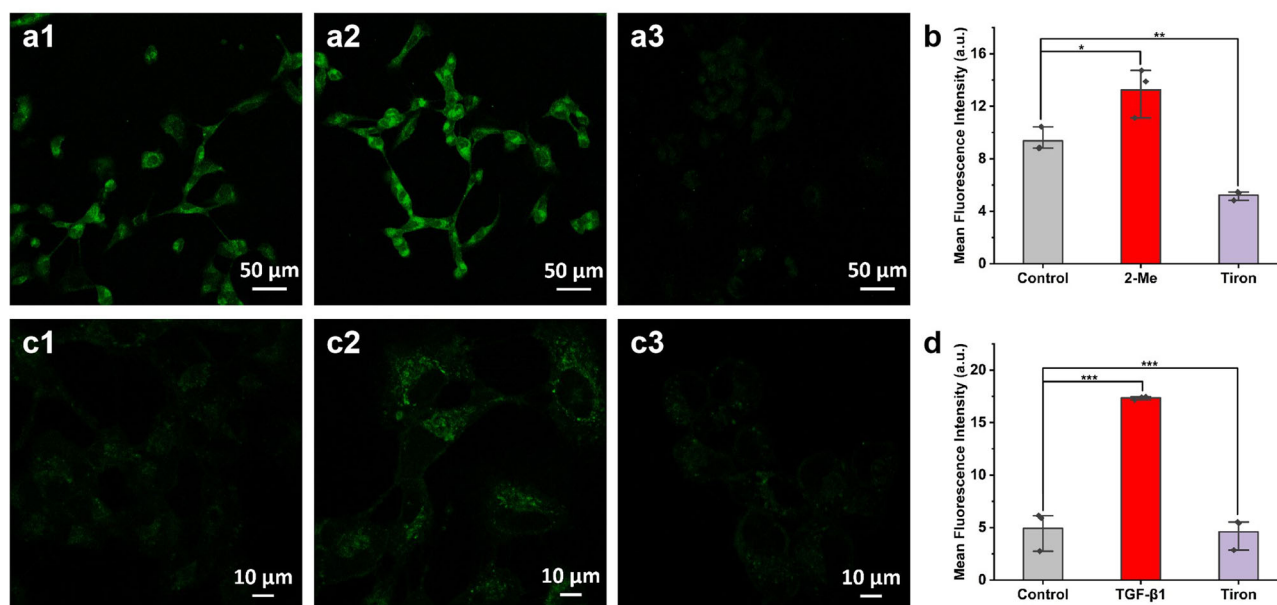


**Fig. 3** |  $O_2^{\cdot-}$  fluorescence imaging of LX-2 cells. **a**  $O_2^{\cdot-}$  fluorescence imaging of endogenous  $O_2^{\cdot-}$  in LX-2 cells. a1: control; a2: 2-Me ( $0.1 \mu\text{g mL}^{-1}$ ) for 15 min; a3: after 2-Me incubation, Tiron ( $10 \mu\text{M}$ ) was added and incubated for 30 min. **c**  $O_2^{\cdot-}$  fluorescence imaging of LX-2 cell activation. c1: control; c2: TGF- $\beta$ 1 ( $5 \text{ ng mL}^{-1}$ ) was

**The activation degrees of HSCs and the levels of intracellular  $O_2^{\cdot-}$**   
Next, the relationship between the activation degrees of HSCs and the  $O_2^{\cdot-}$  levels was explored by the established imaging method. To build the HSCs with varying activation degrees, LX-2 cells were pretreated with different stimulation conditions. As illustrated in Fig. 4, with the increasing of concentration or incubation time, the stronger fluorescence was observed. The above data revealed that the activation degree of HSCs was positively correlated with  $O_2^{\cdot-}$  level.

### $O_2^{\cdot-}$ imaging in mouse HSCs with different activation degrees

Encouraged by the results of the cell experiments, we continued to explore the potential of TPH applications in vivo. The mice with various levels of aHSCs were obtained by intraperitoneal injection carbon tetrachloride ( $\text{CCl}_4$ ) solution (Supplementary Fig. 16)<sup>10,24</sup>. Next, TPH was injected intraperitoneally into the mice before confocal microscope imaging. Compared with the control groups, brighter fluorescence signals were observed in mice with more aHSCs (Fig. 5a–c). These meant that the levels of  $O_2^{\cdot-}$  were increased in mice with aHSCs. Of note, the fluorescence intensities were enhanced 3.0-fold (2 weeks), 4.7-fold (4 weeks), and 10.6-fold (6 weeks), respectively. These findings revealed that as the activation degree of mouse HSCs increased, the  $O_2^{\cdot-}$  levels in HSCs enhanced. Finally, D-penicillamine (D-pen) and tocopherol (VE) were used to inhibit the activation of HSCs<sup>25,26</sup>. A weaker fluorescence was observed in mice with D-pen or VE treated than in mice with  $\text{CCl}_4$  only (Fig. 5d and Supplementary Fig. 17). This result suggested that inhibiting the activation of mouse HSCs could reduce the concentration of  $O_2^{\cdot-}$ . Collectively, all these data implied that TPH could be used for the detection of  $O_2^{\cdot-}$  in mouse HSCs. With the help of TPH, we find that aHSCs produced the excessive  $O_2^{\cdot-}$  in mice.

### The $O_2^{\cdot-}$ level and the immunosuppressive ability of HCC microenvironment

Researches established a closely link between  $O_2^{\cdot-}$  and the immunosuppressive microenvironment of HCC<sup>15,27</sup>. The anti-tumor activity of  $\text{CD8}^+$  T cells inside HCC is affected by ROS<sup>28–30</sup>. Considering the excessive  $O_2^{\cdot-}$  in the aHSCs of mice, we investigated the relationship between  $O_2^{\cdot-}$  in aHSCs and the activity of  $\text{CD8}^+$  T cells in HCC mice. We constructed orthotopic

incubated for 12 h; c3: TGF- $\beta$ 1 was incubated and Tiron ( $10 \mu\text{M}$ ) was added for 30 min. **b, d** Fluorescence intensities of (a) and (c). Scale bar =  $50 \mu\text{m}$  (a) or  $10 \mu\text{m}$  (c). The data were expressed as mean  $\pm$  SD,  $n = 3$ . \* $p < 0.01$ , \*\* $p < 0.05$ , \*\*\* $p < 0.001$  compared to the control group.

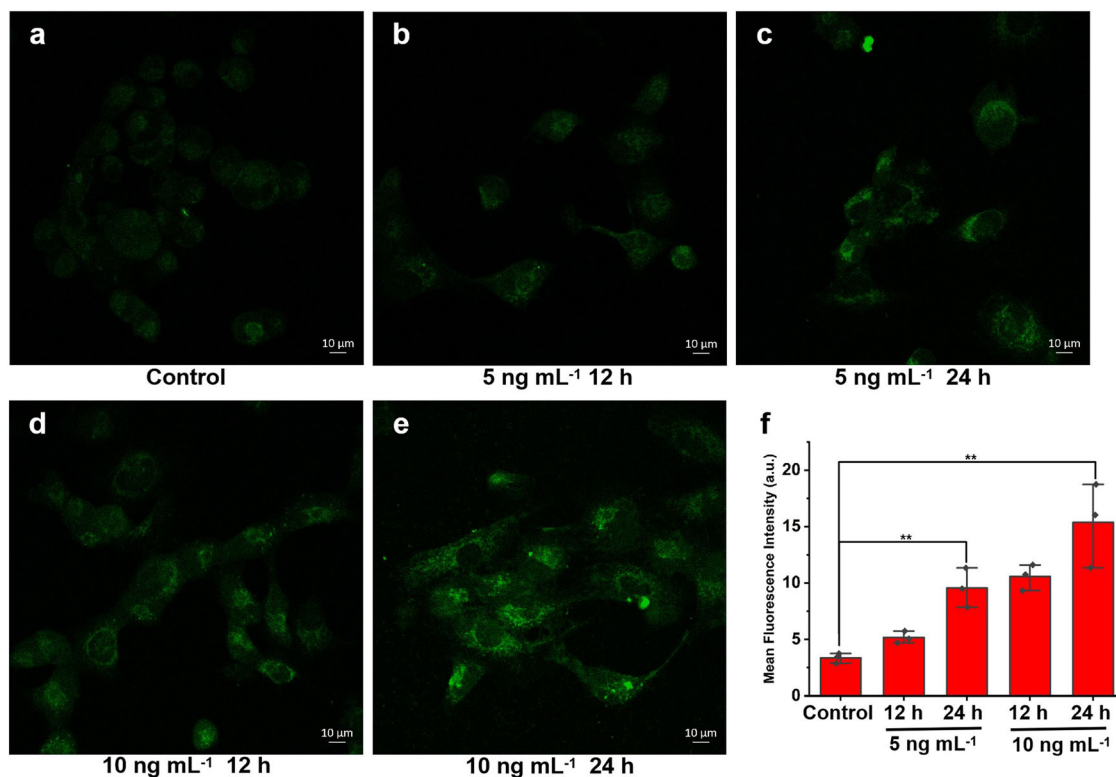


**Fig. 4** |  $O_2^-$  fluorescence imaging of LX-2 cells with different degrees of activation. **a–e** The LX-2 cells were incubated with different TGF- $\beta$ 1 concentrations or times. **f** Fluorescence intensities of **a–e**. Scale bar = 10  $\mu$ m. The data were expressed as mean  $\pm$  SD,  $n = 3$ . **\*\*** $p < 0.05$  compared to the control group.

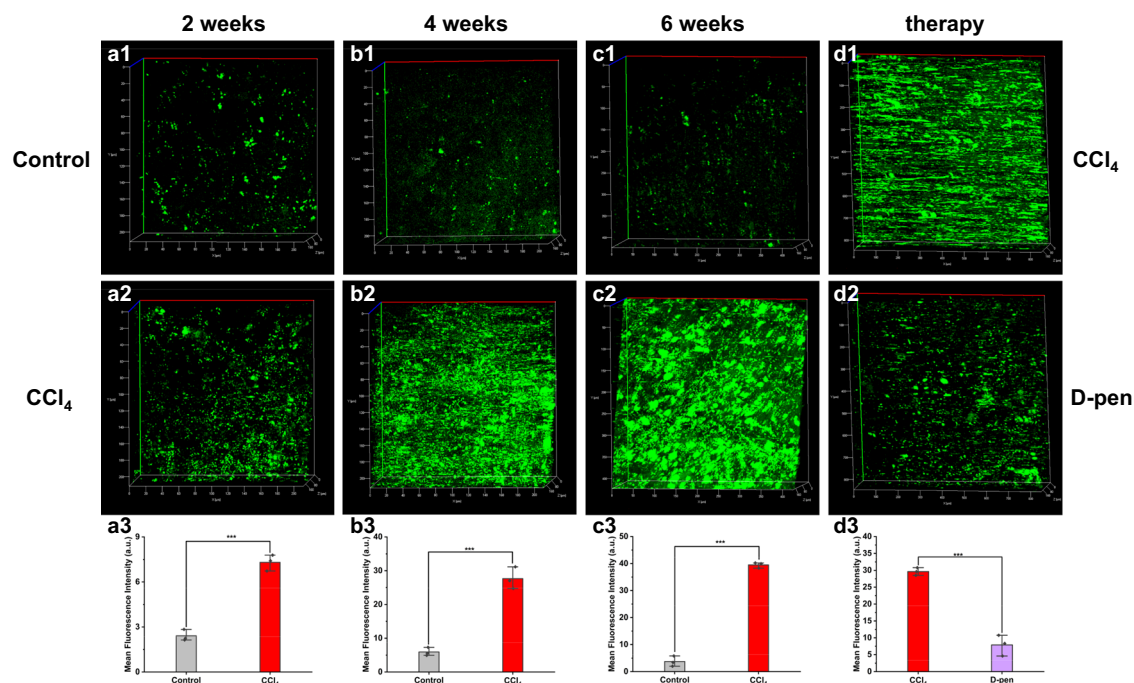


**Fig. 5** | Fluorescence imaging of mice with different levels of HSCs activation. **a–c** Mice were intraperitoneally injected with olive oil or CCl<sub>4</sub> solution for 2, 4, and 6 weeks, respectively. Control: olive oil; CCl<sub>4</sub>: CCl<sub>4</sub> solution. **d** Fluorescence imaging of mice with inhibition of HSCs activation. The mice were first given CCl<sub>4</sub> solution

for 6 weeks, followed by 2 weeks of either stroke-physiological saline solution or D-pen. The data were expressed as mean  $\pm$  SD,  $n = 3$ . **\*\*\*** $p < 0.001$  compared to the control group.

mouse models of HCC containing quiescent-HSCs or aHSCs, and performed fluorescence imaging and immunofluorescence imaging. As shown in Fig. 6a, c, the fluorescence intensities of aHSCs–HCC mice were significantly higher than that of control HCC mice. On the contrary, the proportions of CD8<sup>+</sup> T cells around the tumor were decreased in aHSCs–HCC mice. This suggests a negative correlation between the two biological events: inhibition of HSCs activation decreased the level of O<sub>2</sub><sup>•-</sup> and increased the proportion of CD8<sup>+</sup> T cells around the tumor (Fig. 6b, d and Supplementary Figs. 18–20). These results attested that the O<sub>2</sub><sup>•-</sup> level in HSCs was positively correlated with the immunosuppressive ability of the HCC microenvironment.

It is important that the tumor volume and weight of aHSCs–HCC mice were significantly higher than those of control HCC mice. Meanwhile, using D-pen or VE to reduce the degree of HSCs activation could obviously inhibit the growth of group tumor (Supplementary Fig. 21). This suggests that aHSCs can promote tumor growth. To prove that immune evasion is primarily induced by ROS production, we performed experiments to validate the role of ROS on immune evasion. The experimental results showed that the tumor volume and weight of the mice in the experimental group were smaller compared to the control group (Supplementary Fig. 22). This indicates that scavenging ROS can inhibit tumor growth to a certain extent. All in all, we found that the

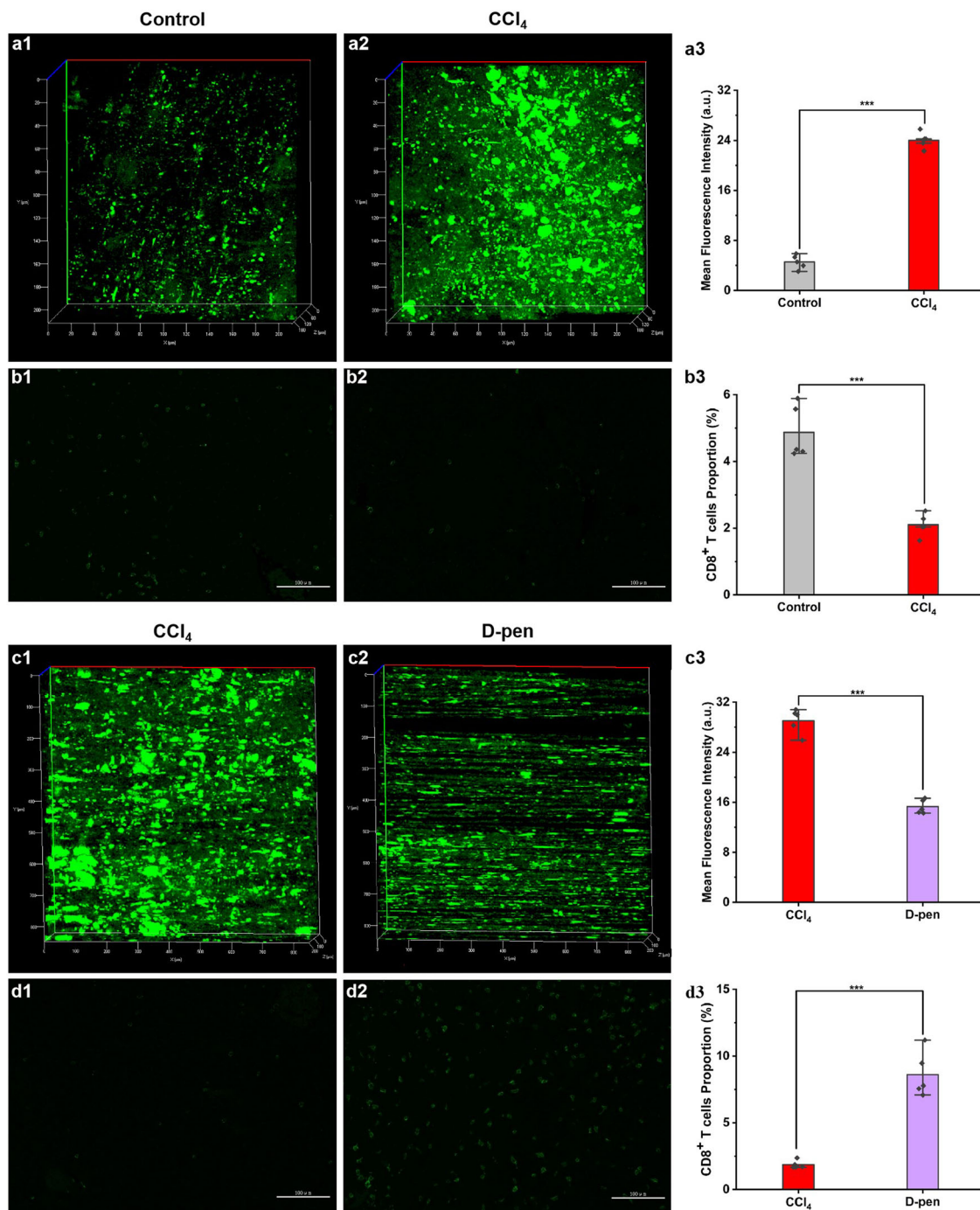


**Fig. 6** | O<sub>2</sub><sup>•-</sup> imaging and immunofluorescence staining of HCC mouse models with varying degrees of HSCs activation. **a, b** O<sub>2</sub><sup>•-</sup> imaging and immunofluorescence staining of ordinary HCC mice and HCC mice with aHSCs. **c, d** O<sub>2</sub><sup>•-</sup>

imaging and immunofluorescence staining of HCC mice with the inhibited aHSCs by D-pen.  $\lambda_{ex} = 800$  nm,  $\lambda_{em} = 450-550$  nm. Scale bar = 100  $\mu$ m. The data were expressed as mean  $\pm$  SD,  $n = 5$ . \*\*\* $p < 0.001$  compared to the control group.

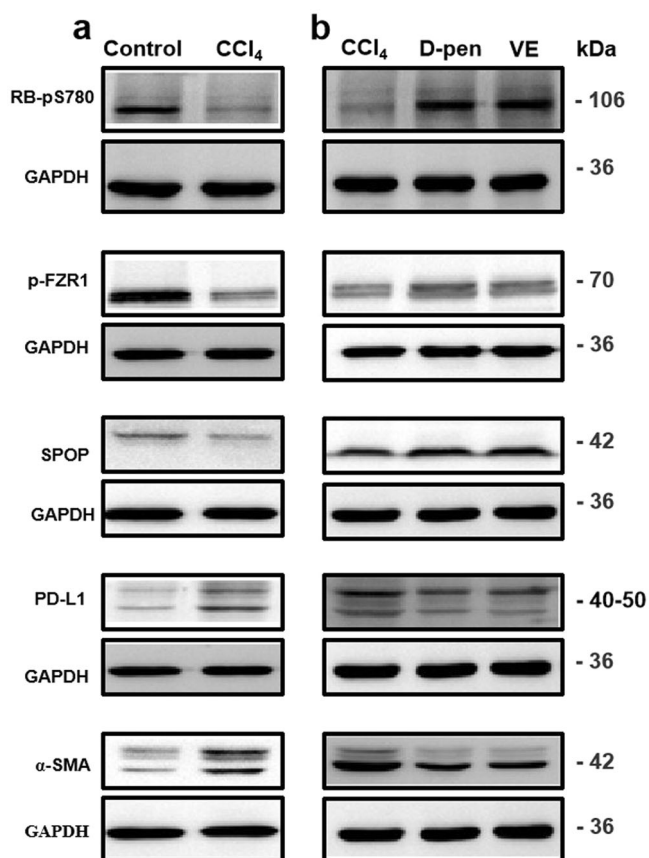


**Fig. 7 | Western blotting of mouse HCC models with different activation levels of HSCs. a** Ordinary HCC mice and HCC mice with aHSCs. **b** HSCs activation was inhibited in HCC mice.

excess  $O_2^{\cdot-}$  generated by the aHSCs enhanced the immunosuppressive ability of the HCC microenvironment, which in turn affects the growth and development of tumor in mice.

### Mechanism of immune evasion mediated by HSCs $O_2^{\cdot-}$ in HCC

Inspired by the above-mentioned exciting findings, we explored the molecular mechanism by which  $O_2^{\cdot-}$  regulates the immune evasion of HCC. In view of upregulation of PD-L1 resulting in immune evasion, we first investigated the expression of PD-L1 during the activation of HSCs. As shown in Fig. 7, we found an obvious upregulation of PD-L1 after HSCs were activated in orthotopic mouse models of HCC. Meanwhile, inhibiting the activation of HSCs led to a distinctly downregulation of PD-L1. Collectively, these results demonstrated that PD-L1 was involved in aHSCs-mediated immune evasion of HCC. The PD-L1 blocking antibody treatment experiments results showed that the tumor volume and weight of mice in the PD-L1 group were significantly reduced (Supplementary Fig. 23). This result suggests that the use of PD-L1 inhibitors can significantly inhibit the growth of tumor in mice, revealing the essential role of PD-L1 in immune evasion.

Next, we explored the signaling pathway leading to the expression change of PD-L1 in aHSCs. Previous studies have indicated that CDK4 could regulate the expression of PD-L1 through the CDK4/p-FZR1/SPOP/PD-L1 mechanism<sup>31</sup>. Therefore, we analyzed the effects of changes in HSCs status on CDK4 activity and related molecular levels. Compared with control HCC mice, we noted that CDK4 activity and p-FZR1 levels were decreased after HSCs activation. Low p-FZR1 levels could induce SPOP protein degradation and ultimately promote the upregulation of PD-L1 level (Fig. 7a). In addition, inhibition of HSCs activation could increase CDK4 activity and decrease PD-L1 expression level (Fig. 7b). Similarly, clearance of ROS produced by hepatic stellate cell activation

can regulate CDK4 activity and PD-L1 levels. These results elucidated that the mechanism of CDK4 mediating PD-L1 was regulated by the activity of HSCs.

However, what cause the change of CDK4 activity remains unknown. Previous reports suggest that  $O_2^{\cdot-}$  can damage protein activity by oxidizing amino acid residues<sup>17</sup>. Therefore, we hypothesized that  $O_2^{\cdot-}$  in aHSCs might damage CDK4 activity, thereby promoting the immune evasion of HCC. To put our hypothesis to the test, we conducted proteomic analyses through LC-MS/MS to investigate the post-translational modifications of CDK4 by  $O_2^{\cdot-}$ . As shown in Fig. 8, three histidine residues (H30, H68, and H95)<sup>32,33</sup> in the active region of CDK4 were oxidized, which should be responsible for the inactivation of CDK4. Based on the above experimental results, we finally proposed a new detailed mechanism by which HSCs promote the immune evasion of HCC. The excess  $O_2^{\cdot-}$  produced by aHSCs damaged the activity of CDK4, increased the level of PD-L1, and finally promoted the immune evasion of HCC.

### Discussion

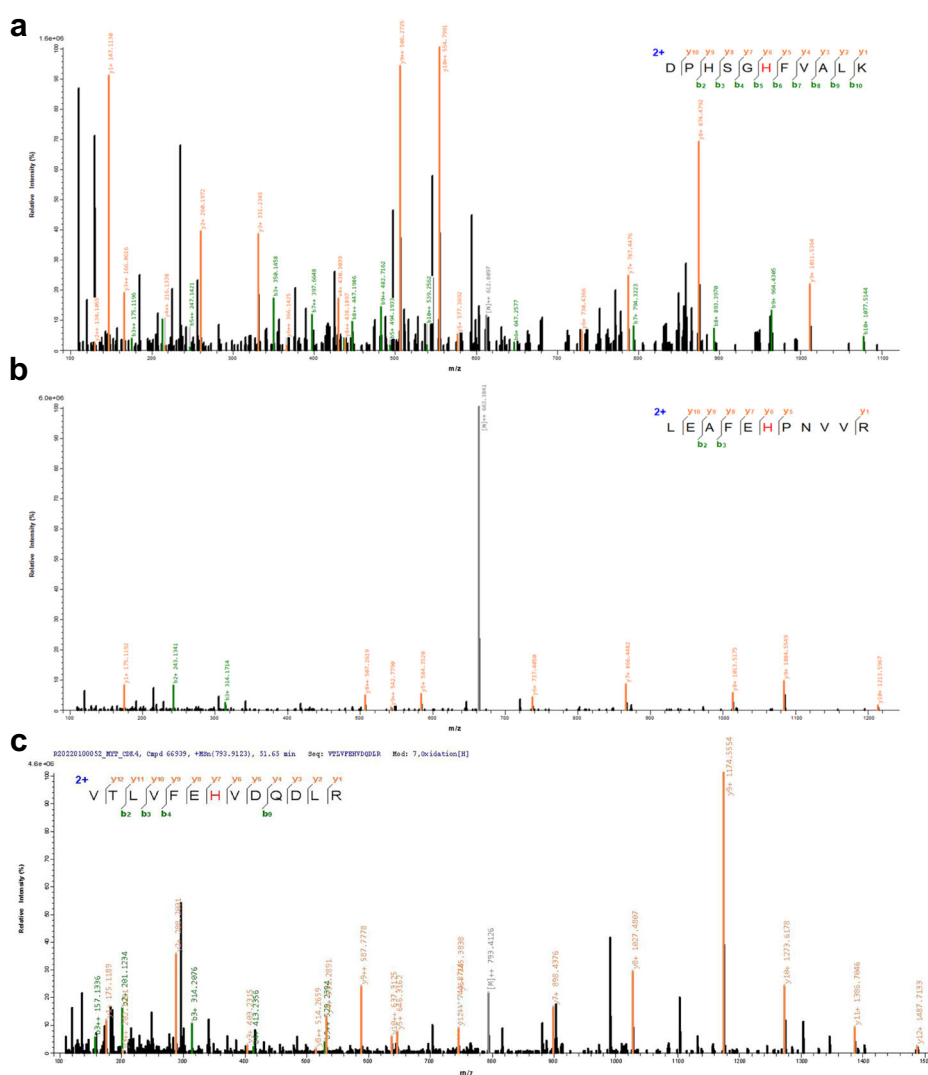
The immunomodulatory role played by HSCs during HCC development has been widely discussed. It is known that HSCs can produce large amounts of ROS when activated, but little is known about their role. Based on the important impact of ROS in cancer development, we analyzed the role of ROS within HSCs in the immune evasion of HCC. Under oxidative stress conditions, the intracellular electron transport chain generates the first ROS- $O_2^{\cdot-}$ , which is a precursor of several ROS and has a remarkable influence in biological signal transduction. However, it is not clear about how  $O_2^{\cdot-}$  within HSCs affects downstream bioactive molecules in relation to immune evasion from HCC. Utilizing the probe TPH, we observed a positive correlation between the level of  $O_2^{\cdot-}$  in HSCs and immune evasion of HCC. This finding provides strong evidence that ROS in HSCs promotes immune evasion from HCC.

It has been reported that activated-HSCs are able to help tumor cells immune evasion by upregulate PD-L1, but its regulatory mechanism is unclear. Meanwhile, some researchers have found a link between ROS and PD-L1. Using fluorescence imaging, the elevated levels of  $O_2^{\cdot-}$  were found in cells and in vivo. This result prompted us to explore whether  $O_2^{\cdot-}$  within HSCs can regulate the expression of PD-L1 during oxidative stress. Therefore, we analyzed the relationship between  $O_2^{\cdot-}$  and PD-L1 in detail. The results of western blot experiments displayed that inducing  $O_2^{\cdot-}$  overproduction could increase the level of PD-L1. Meanwhile, excess  $O_2^{\cdot-}$  could significantly promote the growth of HCC in mice. On the contrary, the level of PD-L1 was significantly reduced and the growth of HCC was effectively delayed by decreased  $O_2^{\cdot-}$ . In conclusion, we found that  $O_2^{\cdot-}$  within HSCs can upregulate intracellular PD-L1, which ultimately leads to immune evasion from HCC.

It was found that the expression of PD-L1 was regulated by CDK4. Numerous experiments have shown that excess  $O_2^{\cdot-}$  can damage DNA and disrupt protein structure, thus affecting the normal physiological functions of organisms. We were interested in whether  $O_2^{\cdot-}$  regulates CDK4 activity. The western blot experiments revealed that excess  $O_2^{\cdot-}$  could reduce the levels of molecules downstream of CDK4. In contrast, the phenomenon disappeared when  $O_2^{\cdot-}$  was removed. The above results suggest that excess  $O_2^{\cdot-}$  within HSCs can increase PD-L1 levels by decreasing CDK4 activity. The results of proteomics analysis experiments further indicated that excess  $O_2^{\cdot-}$  could oxidize amino acid residues in the CDK4 active site. These data convincingly suggest that  $O_2^{\cdot-}$  in HSC induces upregulation of PD-L1 levels by impairing CDK4 activity, and eventually lead to immune evasion. In conclusion, we provided a signaling pathway for the immune evasion of HCC mediated by  $O_2^{\cdot-}$  within HSCs.

In order to explore the role of  $O_2^{\cdot-}$  in HSCs in the immune evasion of HCC, we developed a two-photon fluorescence probe TPH for specific imaging detection of  $O_2^{\cdot-}$ . Using TPH, we observed the increase of  $O_2^{\cdot-}$  during HSCs activation in cells and in vivo. Notably, we found that the

**Fig. 8 | Protein mass spectrometry analysis. a His 30. b His 68. c His 95.**



immunosuppressive ability of the HCC microenvironment was correlated with the activation status of HSCs. Further studies indicated that the excess  $O_2^{\cdot-}$  generated HSCs modified the functional regions of CDK4, resulting in the inactivation of CDK4. Subsequently, the phosphorylation of FZR1 decreased, and caused to more SPOP degraded. The decrease of SPOP led to the increase of PD-L1 in HCC mice, conclusively inducing immune evasion (Fig. 9). This work provided a molecular mechanism by which  $O_2^{\cdot-}$  in HSCs mediated immune evasion from HCC. We propose that this work can provide a supplement to understanding the occurrence and development of HCC. Meanwhile, it is expected to provide new ideas for immunotherapy methods for HCC.

## Methods

### Ethical statement

All animal care and experimental protocols complied with the Animal Management Rules of the Ministry of Health of the People’s Republic of China and were approved by the Animal Care Committee of Shandong Normal University (AECCSDNU2022023).

### Measurement of two-photon cross sections

The two-photon absorption cross sections  $\delta$  were determined using the femtosecond (fs) fluorescence measurement technique. TPH was dissolved in cell lysis buffer at a concentration of 40  $\mu$ M, and then the TP-excited fluorescence spectra were measured at 800 nm. Fluorescein ( $1.0 \times 10^{-4}$  M, pH = 11) whose TP properties have been well

characterized in the literature, was used as the reference. The value of  $\delta$  was calculated using the following equation.

$$\delta_s = \delta_r \frac{\Phi_r C_r n_r F_s}{\Phi_s C_s n_s F_r} \quad (1)$$

The subscripts  $s$  and  $r$  refer to the sample and the reference material, respectively.  $\delta$  is the TP absorption cross-sectional value,  $C$  is the concentration of the solution,  $n$  is the refractive index of the solution,  $F$  is the TP-excited fluorescence intensity, and  $\Phi$  is the fluorescence quantum yield.

### Cell culture

LX-2 cells were purchased from Procell Life Science & Technology Co., Ltd. (Wuhan, China), and cultured in DMEM medium with 10% fetal bovine serum, 1% streptomycin, and 1% penicillin. The cells were placed in an MCO-15AC incubator (Sanyo, Tokyo, Japan) with culture parameters of 37 °C, 5% CO<sub>2</sub>, and 95% air. Two days before the cell imaging experiment, we digested the cells with trypsin and put an appropriate amount of cells into the culture dish for the convenience of the subsequent experimental operation.

### Cytotoxicity assays

The cytotoxicity of 2-(2-methoxy-4-nitrobenzene)-3-(4-nitrobenzene)-5-(2,4-disulfonylbenzene)-2h-tetrazole monosodium salt (CCK8) was tested. LX-2 cells were inoculated on 96-well plates with a concentration of  $1 \times 10^5$

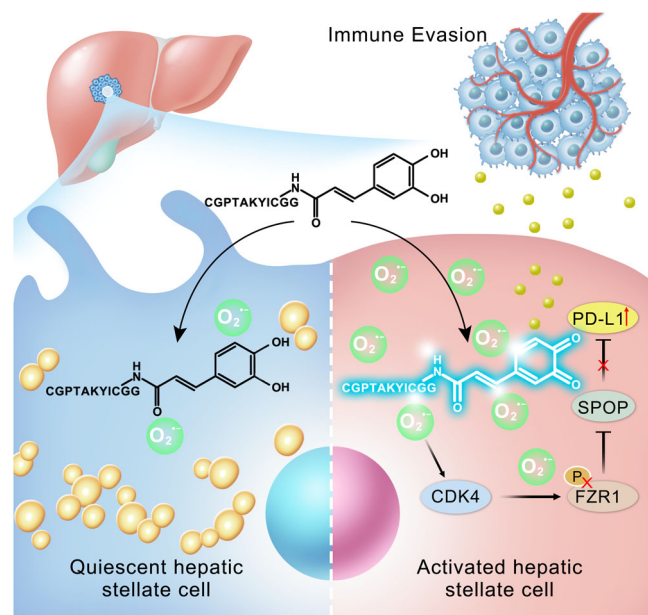


**Fig. 9 | Signal pathway of HCC immune evasion mediated by  $O_2^{\cdot-}$  in HSCs.** HSCs produce large amounts of  $O_2^{\cdot-}$  upon activation. Excessive  $O_2^{\cdot-}$  damages the active region of CDK4, preventing CDK4 from phosphorylating downstream FZR1. Unphosphorylated FZR1 prevents SPOP from degrading PD-L1, which raises PD-L1 levels.

cell pore<sup>-1</sup> and placed in an incubator for 24 h. Then, cells were incubated with different concentrations of probes for 12 h. The cells were rinsed with PBS, followed by 10  $\mu$ L CCK8 solution and 90  $\mu$ L medium were added to per well. After 1 h, the absorbance at 450 nm was measured by enzyme-labeled instrument, and the survival rate of cells was calculated.

### Mice

All male C57 mice (age: 4–6 weeks; average weight:  $20 \pm 2$  g) were purchased from Jinan Pengyue Experimental Animal Breeding Company Limited. The purchased 4–6 weeks C57BL/6 mice were placed in the animal house with 12 h light to ensure adequate water and food for the mice. After a week of adaptation, the mice were randomly grouped to construct mouse models of HSCs with different activation degrees and liver cancer models of HSCs with different activation degrees, respectively.

### The mouse models with various levels of aHSCs

Mice were intraperitoneally injected with olive oil or  $CCl_4$  solution ( $1.0 \text{ mL kg}^{-1}$ ) twice a week for 2, 4, and 6 weeks, respectively. Mice in the treatment group were injected with D-pen ( $100 \text{ mg kg}^{-1}$ ) or vitamin E ( $100 \text{ mg kg}^{-1}$ ) twice a week for 2 weeks after 6 weeks of  $CCl_4$  solution.

### The orthotopic mouse models of HCC containing quiescent-HSCs or aHSCs

Mice were intraperitoneally injected with olive oil or  $CCl_4$  solution ( $1.0 \text{ mL kg}^{-1}$ ) twice a week for 6 weeks, and then the orthotopic mouse models of HCC were constructed. Mice in the treatment group were injected with D-pen ( $100 \text{ mg kg}^{-1}$ ) or VE ( $100 \text{ mg kg}^{-1}$ ) for 2 weeks after 6 weeks of  $CCl_4$  solution, and then the orthotopic mouse models of HCC were constructed.

### Fluorescence imaging experiments in vivo

In vivo imaging experiments, TPH was first injected intraperitoneally into model mice with  $0.62 \text{ mg kg}^{-1}$ . After 30 min, the mice were injected intraperitoneally to numb them, and the mice were opened. The fluorescence imaging was performed using a two-photon fluorescence imaging microscope at an excitation wavelength of 800 nm.

### Proteomic analysis

The CDK4 was dissolved in the appropriate buffer (50 mM Tris, pH = 8.0). Then, 1 mM superoxide anion ( $O_2^{\cdot-}$ ) was added, and incubated at 37 °C for 2 h. CDK4 was trypsin digested, and the peptides were isolated from the hydrolysate by solid phase extraction on the C-18 column. Proteomic analysis was performed by LC-MS/MS.

### Statistics and reproducibility

The data were analyzed using Origin Pro 2021 (64-bit). Student's *t* test was used to evaluate the differences between the data. *P* values < 0.05 were considered statistically significant. It was defined as \**P* < 0.05, \*\**P* < 0.01, and \*\*\**P* < 0.001.

### Reporting summary

Further information on research design is available in the Nature Portfolio Reporting Summary linked to this article.

### Data availability

All the data generated in this study are provided in the Supplementary Information/Source Data file. There are no restrictions on data availability in the current work. The mass spectrometry proteomics data have been deposited to the ProteomeXchange Consortium (<http://proteomecentral.proteomexchange.org>) via the iProX partner repository<sup>34,35</sup> with the dataset identifier PXD051328.

Received: 31 December 2022; Accepted: 25 April 2024;

Published online: 10 May 2024

### References

- Craig, A. J., Von Felden, J., Garcia-Lezana, T., Sarcognato, S. & Villanueva, A. Tumour evolution in hepatocellular carcinoma. *Nat. Rev. Gastroenterol. Hepatol.* **17**, 139–152 (2020).
- Wang, C., Cao, Y., Yang, C., Bernards, R. & Qin, W. Exploring liver cancer biology through functional genetic screens. *Nat. Rev. Gastroenterol. Hepatol.* **18**, 690–704 (2021).
- Llovet, J. M. et al. Immunotherapies for hepatocellular carcinoma. *Nat. Rev. Clin. Oncol.* **19**, 151–172 (2022).
- Sangro, B., Sarobe, P., Hervás-Stubbs, S. & Melero, I. Advances in immunotherapy for hepatocellular carcinoma. *Nat. Rev. Gastroenterol. Hepatol.* **18**, 525–543 (2021).
- Rizvi, S., Wang, J. & El-Khoueiry, A. B. Liver cancer immunity. *Hepatology* **73**, 86–103 (2021).
- Molina-Sánchez, P. et al. Cooperation between distinct cancer driver genes underlies intertumor heterogeneity in hepatocellular carcinoma. *Gastroenterology* **159**, 2203–2220 (2020).
- Friedman, S. L. Hepatic stellate cells: protean, multifunctional, and enigmatic cells of the liver. *Physiol. Rev.* **88**, 125–172 (2008).
- Pellicoro, A., Ramachandran, P., Iredale, J. P. & Fallowfield, J. A. Liver fibrosis and repair: immune regulation of wound healing in a solid organ. *Nat. Rev. Immunol.* **14**, 181–194 (2014).
- Friedman, S. L. Mechanisms of hepatic fibrogenesis. *Gastroenterology* **134**, 1655–1669 (2008).
- Tsuchida, T. & Friedman, S. L. Mechanisms of hepatic stellate cell activation. *Nat. Rev. Gastroenterol. Hepatol.* **14**, 397–411 (2017).
- Myojin, Y. et al. Hepatic stellate cells in hepatocellular carcinoma promote tumor growth via growth differentiation factor 15 production. *Gastroenterology* **160**, 1741–1754 (2021).
- Coulouarn, C. et al. Hepatocyte–stellate cell cross-talk in the liver engenders a permissive inflammatory microenvironment that drives progression in hepatocellular carcinoma hepatocyte–stellate cell cross-talk in liver cancer. *Cancer Res.* **72**, 2533–2542 (2012).
- Han, S. et al. Activated hepatic stellate cells promote hepatocellular carcinoma cell migration and invasion via the activation of FAK-MMP9 signaling. *Oncol. Rep.* **31**, 641–648 (2014).

14. Xiao, H. et al. Versatile fluorescent probes for imaging the superoxide anion in living cells and in vivo. *Angew. Chem., Int. Ed.* **132**, 4244–4258 (2020).
15. Zhang, Y. et al. ROS play a critical role in the differentiation of alternatively activated macrophages and the occurrence of tumor-associated macrophages. *Cell Res.* **23**, 898–914 (2013).
16. Denk, W., Strickler, J. H. & Webb, W. W. Two-photon laser scanning fluorescence microscopy. *Science* **248**, 73–76 (1990).
17. Ding, Q. et al. Oxidative damage of tryptophan hydroxylase-2 mediated by peroxisomal superoxide anion radical in brains of mouse with depression. *J. Am. Chem. Soc.* **142**, 20735–20743 (2020).
18. Zhang, W. et al. Dynamic and reversible fluorescence imaging of superoxide anion fluctuations in live cells and in vivo. *J. Am. Chem. Soc.* **135**, 14956–14959 (2013).
19. Guo, Z. et al. Specific hepatic stellate cell-penetrating peptide targeted delivery of a KLA peptide reduces collagen accumulation by inducing apoptosis. *J. Drug Target.* **25**, 715–723 (2017).
20. Huang, P., Feng, L., Oldham, E. A., Keating, M. J. & Plunkett, W. Superoxide dismutase as a target for the selective killing of cancer cells. *Nature* **407**, 390–395 (2000).
21. Zhou, Y., Hileman, E. O., Plunkett, W., Keating, M. J. & Huang, P. Free radical stress in chronic lymphocytic leukemia cells and its role in cellular sensitivity to ROS-generating anticancer agents. *Blood J. Am. Soc. Hematol.* **101**, 4098–4104 (2003).
22. Du, Y., Miller, C. M. & Kern, T. S. Hyperglycemia increases mitochondrial superoxide in retina and retinal cells. *Free Radic. Biol. Med.* **35**, 1491–1499 (2003).
23. Kharbanda, K. K. et al. Transforming growth factor- $\beta$  induces contraction of activated hepatic stellate cells. *J. Hepatol.* **41**, 60–66 (2004).
24. Trautwein, C., Friedman, S. L., Schuppan, D. & Pinzani, M. Hepatic fibrosis: concept to treatment. *J. Hepatol.* **62**, S15–S24 (2015).
25. Epstein, O. et al. D-penicillamine treatment improves survival in primary biliary cirrhosis. *Lancet* **317**, 1275–1277 (1981).
26. Vilar-Gomez, E. et al. Vitamin E improves transplant-free survival and hepatic decompensation among patients with nonalcoholic steatohepatitis and advanced fibrosis. *Hepatology* **71**, 495–509 (2020).
27. Xu, Q. et al. NADPH oxidases are essential for macrophage differentiation. *J. Biol. Chem.* **291**, 20030–20041 (2016).
28. Jackson, S. H., Devadas, S., Kwon, J., Pinto, L. A. & Williams, M. S. T cells express a phagocyte-type NADPH oxidase that is activated after T cell receptor stimulation. *Nat. Immunol.* **5**, 818–827 (2004).
29. Kwon, J. et al. The nonphagocytic NADPH oxidase Duox1 mediates a positive feedback loop during T cell receptor signaling. *Sci. Signal.* **3**, ra59 (2010).
30. Devadas, S., Zaritskaya, L., Rhee, S. G., Oberley, L. & Williams, M. S. Discrete generation of superoxide and hydrogen peroxide by T cell receptor stimulation: selective regulation of mitogen-activated protein kinase activation and fas ligand expression. *J. Exp. Med.* **195**, 59–70 (2002).
31. Zhang, J. et al. Cyclin D–CDK4 kinase destabilizes PD-L1 via cullin 3–SPOP to control cancer immune surveillance. *Nature* **553**, 91–95 (2018).
32. Jeffrey, P. D., Tong, L. & Pavletich, N. P. Structural basis of inhibition of CDK–cyclin complexes by INK4 inhibitors. *Genes Dev.* **14**, 3115–3125 (2000).
33. Day, P. J. et al. Crystal structure of human CDK4 in complex with a D-type cyclin. *Proc. Natl Acad. Sci. USA* **106**, 4166–4170 (2009).
34. Ma, J. et al. iProX: an integrated proteome resource. *Nucleic Acids Res.* **47**, D1211–D1217 (2019).
35. Chen, T. et al. iProX in 2021: connecting proteomics data sharing with big data. *Nucleic Acids Res.* **50**, D1522–D1527 (2021).

## Acknowledgements

This work was supported by the National Natural Science Foundation of China (22134004, 22074083, 21927811), the Key Research and Development Program of Shandong Province (2018YFJH0502), National Science Foundation of Shandong Province of China (ZR2020ZD17), Youth Fund of Natural Science Foundation of Shandong Province (ZR2021QB042), Taishan Scholars (Tsqn201812125), National Youth Qihuang Scholar Training Program, Shandong Province Traditional Chinese Medicine High Level Talent Cultivation Project and Key Research and Development Project of Shandong Province (2020CXGX010505).

## Author contributions

X.W., P.L., and B.T. conceived the work. Y.M. and C.W. performed optical characterization experiments and mouse experiments. F.Z. and X.Q. performed cell experiments. X.L. provided technical support. Y.M. and C.W. wrote the original draft. X.W., P.L., and B.T. reviewed and finished the final editing of the manuscript.

## Competing interests

The authors declare no competing interests.

## Additional information

**Supplementary information** The online version contains supplementary material available at <https://doi.org/10.1038/s42003-024-06245-y>.

**Correspondence** and requests for materials should be addressed to Xin Wang, Xia Li, Ping Li or Bo Tang.

**Peer review information** *Communications Biology* thanks the anonymous reviewers for their contribution to the peer review of this work. Primary Handling Editors: Periklis Pantazis, Zhijuan Qiu, and Dario Ummarino.

**Reprints and permissions information** is available at <http://www.nature.com/reprints>

**Publisher's note** Springer Nature remains neutral with regard to jurisdictional claims in published maps and institutional affiliations.

**Open Access** This article is licensed under a Creative Commons Attribution 4.0 International License, which permits use, sharing, adaptation, distribution and reproduction in any medium or format, as long as you give appropriate credit to the original author(s) and the source, provide a link to the Creative Commons licence, and indicate if changes were made. The images or other third party material in this article are included in the article's Creative Commons licence, unless indicated otherwise in a credit line to the material. If material is not included in the article's Creative Commons licence and your intended use is not permitted by statutory regulation or exceeds the permitted use, you will need to obtain permission directly from the copyright holder. To view a copy of this licence, visit <http://creativecommons.org/licenses/by/4.0/>.

© The Author(s) 2024